Correcting for contact geometry in Seebeck coefficient measurements of thin film devices

Stephan van Reenen and Martijn Kemerink

Original Publication:

Stephan van Reenen and Martijn Kemerink, Correcting for contact geometry in Seebeck coefficient measurements of thin film devices, 2014, Organic electronics, (15), 10, 2250-2255.
http://dx.doi.org/10.1016/j.orgel.2014.06.018

Correcting for contact geometry in Seebeck coefficient measurements of thin film devices

Stephan van Reenen[1] and Martijn Kemerink[1,2]

[1] Molecular Materials and Nanosystems, Eindhoven University of Technology, Department of Applied Physics, PO Box 513, 5600 MB Eindhoven, The Netherlands.

[2] Department of Physics, Chemistry and Biology (IFM), Linköping University, SE-58 183, Linköping, Sweden

e-mail: martijn.kemerink@liu.se.

Abstract:

Driven by promising recent results, there has been a revived interest in the thermoelectric properties of organic (semi)conductors. Concomitantly, there is a need to probe the Seebeck coefficient *S* of modestly conducting materials in thin film geometry. Here we show that geometries that seem desirable from a signal-to-noise perspective may induce systematic errors in the measured value of S, S_m, by a factor 3 or more. The enhancement of S_m by the device geometry is related to competing conduction paths outside the region between the electrodes. We derive a universal scaling curve that allows correcting for this and show that structuring the semiconductor is not needed for the optimal electrode configuration, being a set of narrow, parallel strips.

TOC (5x13 cm²):

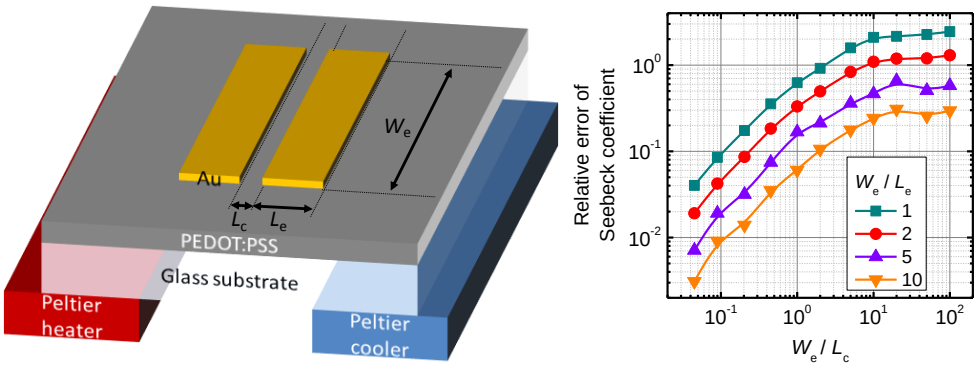

Keywords:

-Thermoelectric generators

-Seebeck coefficient

-Thin films

-PEDOT:PSS

-Device physics

Highlights:

-The effect of device geometry on the measured Seebeck coefficient (S_m) is studied

-Wrong choice in device geometry can lead to errors in S_m as high as a factor 3

-Universal scaling of the errors in S_m is demonstrated, allowing for *a posteriori* correction; analytical calculations confirm its limiting behavior

-Experiments on different device geometries show the same effect

1. Introduction

The use of organic materials for thermoelectric applications[1-16] has rapidly gained popularity in the past few years. Compared to e.g. inorganic materials, organic materials offer relatively low thermal conductivity[17] and good processability and scalability.[2, 11] In combination with the absence of rare elements the latter properties make organic materials potentially relevant for large-area harvesting of (waste) heat. The thermal conductivity is however not the only parameter that defines the quality of a material to be used as thermoelectric generator. This quality is expressed by the thermoelectric figure of merit $ZT = S^2\sigma\ T/\kappa$,[18] where S is the Seebeck coefficient, σ the electrical conductivity, T the absolute temperature, and κ the thermal conductivity. Recent work[2-3, 19] on materials based on poly(3,4-ethylenedioxythiophene) (PEDOT) has shown the potential of doped organic semiconductors for thermoelectric applications and the reported record value of ZT in organic materials has increased up to 0.42,[3] approaching the record value in inorganic materials, ZT = 1.4, in bismuth antimony telluride.

With the field of organic thermoelectrics gaining momentum, it is highly desirable that consistent methodologies to determine ZT are employed. To determine the figure of merit of a material, S, σ and κ need to be determined. In this paper we focus on the measurement of S, and show that, when working in thin-film geometry, Seebeck measurements are particularly prone to suffer from systematic and substantial overestimation of S. It is the purpose of this paper to assist in the design and interpretation of Seebeck measurements on thin organic films.

The Seebeck coefficient is the ratio of the thermovoltage and its driving force, the temperature difference:

$$S = \Delta V/\Delta T. \qquad (1)$$

The magnitude of S is related to the temperature dependence of the Fermi level. An important consequence of this equation is that a small temperature gradient does not necessarily lead to a small thermovoltage as it is its integral, the temperature difference, between the two electrodes that matters. This is in contrast to electrical currents that are driven by voltage gradients, i.e. electric fields. Ideally, voltage probes are therefore infinitely small or otherwise forced to have a constant temperature over their entire area. When not, the thermovoltage becomes ill-defined and erroneous values of S are measured. Triggered by the differences in electrode geometries in recent reports[2-4, 9-14] and our failure to reproduce some of them we here address the errors that can be made in measuring S of thin films with experimentally practical device geometries.

In practice, measurement of S in organic (semi)conductor thin films, that are typically of low to modest conductivity, demands the use of metal electrodes of finite size to monitor the thermovoltage. The reason is that the device impedance, as probed between the electrodes, needs to be small compared to the input impedance of the measurement setup. In literature different electrode geometries are encountered, e.g. long narrow electrodes,[4, 19-20] roughly square electrodes,[3] point-like contacts,[9, 14] and more complex structures.[2, 11] One of the considerations when choosing the contact geometry is the conductivity of the studied material. To improve the signal-to-noise ratio short channels with a large cross-sectional area are preferred. Therefore point contacts are often not feasible to measure Seebeck

coefficients in thin films. For an ideal Seebeck coefficient measurement with finite-sized electrodes current flow is only allowed within the channel between the two electrodes as is the case in Ref. [2]. In other cases,[3-4, 10, 19-21] the electrodes are placed on top of or below a larger semiconducting film, enabling additional current flow outside the channel. When a linear temperature gradient is applied in a region that includes the electrodes, as for practical reasons is commonly done, this electrode layout possibly distorts the measured value of S: Fig. 1 shows a typical experimental geometry in which the thermovoltage ΔV_{23} is smaller than ΔV_{14} as ΔT_{23} is smaller than ΔT_{14}. The intuitive assumption that ΔV_{23} will dominate the measurement need not be correct, as will be quantified below by numerical and analytical calculations and experiments.

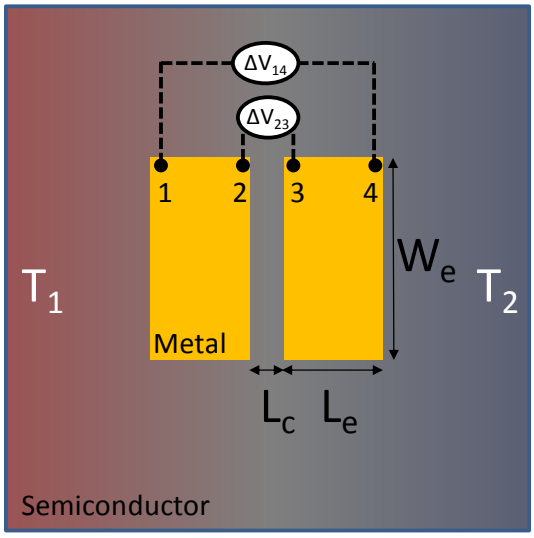

Fig. 1. Schematic layout of the modeled device geometry for Seebeck measurements. Color gradients reflect the temperature profile in the semiconductor.

By means of numerical modeling we show that an inappropriate choice in device geometry can lead to a measured Seebeck coefficient, S_m, that is larger than the actual Seebeck coefficient, S_0, of the studied material by up to a factor 3 in case square-shaped electrodes are used. This enhancement is driven by the larger temperature difference outside the channel, resulting in additional conduction pathways, enhancing the thermovoltage. The difference between S_m and S_0 resulting from this process can be reduced significantly by removal of the active material outside the channel; the use of a set of parallel, narrow line-shaped electrodes; or simply by determination and compensation of the error in S_m, i.e. $S_m - S_0$. The latter is facilitated by the fact that the geometry-induced error in S follows a universal scaling behavior, so the results presented below can be used to correct any experiment conducted with the layout sketched in Fig. 1. The numerical calculations are confirmed in relevant limits by intuitive analytical derivations based on Ohm's law, which prove that the described effect must be present –in fact, finding an independence on geometry should set off alarm bells. Experiments have shown that partial patterning of the active layer outside of the channel indeed results in a better approximation of S_0 by S_m.

2. Materials and Methods

2.1 Computational details:

A top-view of the device geometry considered in the numerical simulations is shown in Fig. 1. The model is used to calculate the thermovoltage which results from a linearly distributed temperature difference $\Delta T = T_2 - T_1$, which is applied across the complete device. Carrier transport is calculated on a 2D rectangular grid by forward integration in time of the Boltzmann transport equation. Poisson's equation is used to calculate the potential after each time step. The electrodes have a fixed potential and hole injection into its neighboring cells is described by setting a fixed, large density of free holes at the contact edges, which is a commonly accepted way to mimic Ohmic contacts. For simplicity, a delta-shaped density of states was used, which is known to give rise to large Seebeck coefficients, $S_0 \approx 340$ µV/K for the used parameters.[22] However, since we are interested in the relative influence of the device geometry, the magnitude of S_0 is irrelevant. To model a doped system like PEDOT:PSS, a fixed density of negatively charged and immobile dopants ($n_{dopant} = 1 \cdot 10^{25}$ m^{-3}) is added to the semiconductor, compensated by the same density of mobile holes. The dimensions of the semiconductor surrounding the contacts were made sufficiently large that further increases did not affect the thermovoltage anymore. More details on the numerical model can be found in the supplementary information part A. Importantly, since relative errors are reported below, the material-specific parameters in the model are of no effect to our conclusions.

2.2 Experimental details:

Devices were prepared on pre-cleaned 1mm thick glass substrates. Electrodes were deposited by thermal evaporation of Cr (5 nm) and Au (100 nm) through a shadow mask in vacuum. Materials to be characterized were spin-cast on top of the substrate. Either one of two variants of doped poly(3,4-ethylenedioxythiophene) (PEDOT) stabilized by poly(styrenesulphonate) (PSS) were characterized: Clevios 4083 and Clevios PH1000 from H.C. Starck. The latter was mixed with 5 vol% DMSO prior to spin coating. After spin coating the layers were dried on a hotplate at 120 °C for 10 minutes. The final layer thickness of the films was ≈ 60 nm. Sample preparation was performed in air.

Measurement of S_m and σ was performed under nitrogen atmosphere (H_2O < 1 ppm and O_2 < 1 ppm) in a glovebox. A Keithley source measure unit 2636 was used to measure both thermovoltages and conductivities. Before measurement samples were annealed again on a hotplate in the glovebox at 120 °C for 10 minutes. The substrate was positioned on two Peltier elements in such a way that a temperature gradient can be established across the substrate. Note that the thermal conductance of the ≈ 100 nm thick electrodes is negligible compared to the thermal conductance of the 1.5 mm thick glass substrate. Consequently, a linear temperature profile can be assumed across the glass substrate between the Peltier elements. Two silicon diodes were used to measure the temperature on each side of the sample. The electrodes were contacted by Au probe needles. The thermovoltage ΔV at a given temperature gradient ΔT was determined by measurement of the zero crossing of the *I*-*V* characteristic. S_m was then determined by fitting the measured ΔV over a range of ΔT with Eq. 1.

3. Results and Discussion

3.1 Numerical calculation of the error in the measured Seebeck coefficient

To study different device geometries by numerical calculations, we varied the aspect ratio of the channel,

$$r_c = \frac{W_e}{L_c}, \tag{2}$$

and the aspect ratio of the electrodes,

$$r_e = \frac{W_e}{L_e}. \tag{3}$$

Eqs. 2 and 3 reflect that the entire problem is scale invariant. The device Seebeck coefficient, S_m, is calculated from Eq. 1 under the (incorrect) assumption that the obtained thermovoltage represents ΔV_{23} (see Fig. 1) and, is plotted in Fig. 2a for different aspect ratios.

The results show that small relative errors result when the channel length L_c is much longer than the electrode length L_e, i.e. when $r_c/r_e \ll 1$. In this limit the relative difference between T_{14} and T_{23}, and hence between V_{14} and V_{23} becomes vanishingly small. In practice this easily leads to such an increase in device impedance that noise and sensitivity become an issue.

For larger channel aspect ratios, the modeling reveals a significant dependence of the measured Seebeck coefficient on the electrode aspect ratio. Large aspect ratio electrodes, i.e. wide and short, (triangles in Fig. 2) clearly result in the most accurate approximation of S_0, whereas square-shaped electrodes (squares in Fig. 2) easily lead to an overestimation of S_0 by a factor >3.

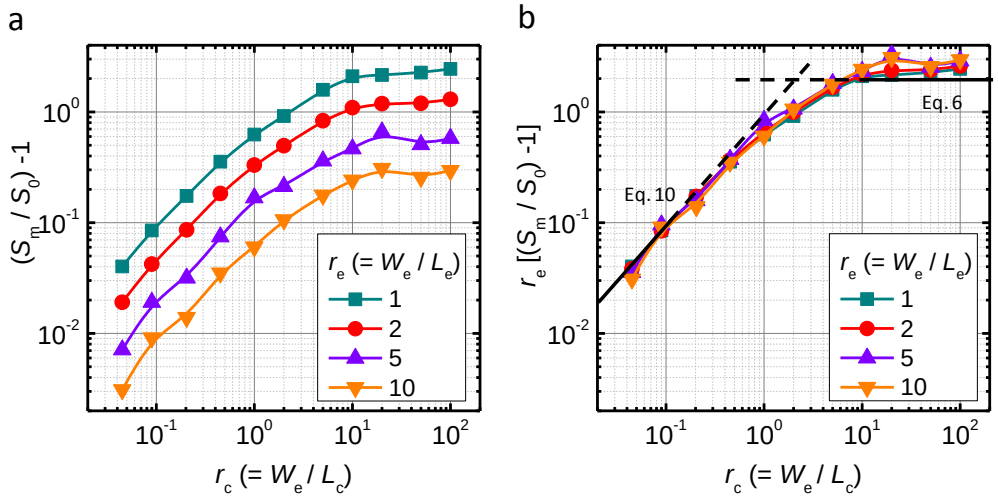

Fig. 2. (a) Relative error in measured Seebeck coefficient for different channel and electrode aspect ratios. The error in the Seebeck coefficient of the device S_m is relative to the true Seebeck coefficient of the modeled semiconductor S_0. b) The relative error in the measured Seebeck coefficient multiplied by the electrode aspect ratio r_e reveals a universal curve. The solid black lines indicate the analytical limits (Eq. 6) and (Eq. 10) discussed in the text.

3.2 Analytical limits for the error in the measured Seebeck coefficient

The relative error in the measured Seebeck coefficient in Fig. 2a is observed to have two limits related to the channel aspect ratio: for $r_c >> 1$, the relative error is roughly constant, whereas for $r_c << 1$ the error is observed to decrease linearly. In the following paragraphs intuitive analytical derivations are given for both these limits to gain understanding regarding the origin of the error in the measured Seebeck coefficient. This derivation is based on Ohm's law.

The thermovoltage that is measured, ($V_{th,m}$), can intuitively be separated into two components: one related to the actual channel potential V_{23} and a spurious one related to the potential V_{14} that drops in the regions outside and far away from the channel. To determine the influence of these different regions, the conductance associated with each contribution should be used as weighting factor:

$$V_{th,m} \sim \frac{V_{23} \cdot G_{23} + V_{14} \cdot G_{14}}{G_{23} + G_{14}}, \tag{4}$$

where $G_{23} = \sigma_{PEDOT} \frac{d \cdot W_e}{L_c}$ is the conductance of the PEDOT in the channel between the electrodes and G_{14} is related to the conductance of the PEDOT outside the channel. d_{PEDOT} is the thickness of the layer which is of no further importance.

First we consider the limit $r_c >> 1$. Suppose the geometry of the electrodes is constant (r_e = constant) and that r_c increases by a reduction of L_c. In the limit $r_c >> 1$, where r_e = constant, both V_{14} and G_{14} can be considered constant as well. G_{23} however increases with decreasing L_c (and increasing r_c) as $1/L_c$, whereas V_{23} decreases linearly. Eq. 4 then predicts that the thermovoltage should decrease linearly as only the denominator increases linearly ($G_{23} >> G_{14}$):

$$V_{th,m} \sim V_{23} + V_{14} \frac{G_{14}}{G_{23}}. \tag{5}$$

The relative error in the thermovoltage then becomes:

$$\frac{V_{th,m}}{V_{23}} - 1 \sim \frac{V_{23}}{V_{23}} + \frac{V_{14}}{V_{23}} \frac{G_{14}}{G_{23}} - 1 = \frac{V_{14}}{V_{23}} \frac{G_{14}}{G_{23}}. \tag{6}$$

As V_{14} and G_{14} can be considered constant for decreasing L_c in the limit $r_c >> 1$, the simultaneously increasing G_{23} and decreasing V_{23} compensate each other, making the relative error constant. This is in agreement with the constant region in Fig. 1b for $r_c >> 1$. The saturation value of about $2/r_e$ can be handwavingly rationalized by a simple square-counting argument as described in the supplementary information part B. An important consequence of this constant relative error is that differential probes, in which S_m is obtained as a function of channel length do not avoid this geometry-related problem as long as the channel remains short.

In the other limit, $r_c << 1$, again Eq. 4 is used as starting point. Now V_{14} can be expressed as:

$$V_{14} = V_{23} + \Delta, \tag{7}$$

where

$$\Delta = 2V_{23}\frac{L_e}{L_c} = 2V_{23}\frac{r_c}{r_e}. \quad (8)$$

Combination of Eqs. 4, 7 and 8 gives the relative error in the thermovoltage, which is linearly related to the Seebeck coefficient:

$$\frac{V_{th,m}}{V_{23}} - 1 = 2\frac{r_c}{r_e}\frac{G_{14}}{G_{23}+G_{14}}. \quad (9)$$

For small r_c, the points 1 and 2 as well as 3 and 4 in Fig. 1 collapse, resulting in $G_{14} = G_{23}$. Hence Eq. (9) reduces to

$$\frac{V_{th,m}}{V_{23}} - 1 = \frac{r_c}{r_e}, \quad (10)$$

which is linear in r_c for constant r_e, in agreement with the numerically calculated relative error in the regime $r_c << 1$ shown in Fig. 2a. In addition we note that the relative error multiplied by the electrode aspect ratio r_e only depends on the channel aspect ratio as is shown in Fig. 2b.

3.3 Experimental verification of geometry influence

To verify the modeled results experimentally, two Seebeck coefficient measurements on PEDOT:PSS (Clevios 4083) with different channel and electrode aspect ratios were performed as shown in Figure 3a and b. For the aspect ratios r_c = 7 and r_e = 7 the measured Seebeck coefficient was found to be 5±2 µV/K. For the aspect ratios r_c = 37.5 and r_e = 0.75 the measured Seebeck coefficient was found to be 22±4 µV/K. This is in quantitative agreement with the numerical model that predicts errors (i.e. S_m/S_0) of respectively ~1.25 and ~3.8 for these geometries. Compensating for the geometry, the values of S_0 are 4±2 µV/K and 6±1 µV/K for r_e = 7 and 0.75, respectively.

Similar measurements on PEDOT:PSS (Clevios PH1000) are shown in Fig. 3d. In addition, the distance between the Au probes contacting the pads was varied to eliminate any probe-related effects. Altering the inter-probe distance clearly has an effect on the resultant value of S_m, which is determined by the temperature difference across the channel and the measured thermovoltage using Eq. (1). Dashed lines are added to indicate the trend of this behavior. At the limit of zero inter-probe distance spurious thermoelectric effects due to the probe-contact interfaces vanish, leaving purely the measured Seebeck coefficient of the PEDOT. Again, the use of electrodes with r_e = 0.75 results in a relatively large error in S_m of approximately a factor 4 compared to a device with r_e = 7. The value of S_m = 30±3 µV/K for r_e = 0.75 is similar to the values obtained in Ref. [3] for a similar device geometry with the same PEDOT:PSS material (Clevios PH1000 from H.C. Starck). Compensating for the geometry, the calculated values of S_0 are 6±2 µV/K and 8±1 µV/K for r_e = 7 and 0.75, respectively. The resistivity values of the PEDOT was determined to be 7.5 and 5.2 µΩ m for the rectangular and square electrode geometry, respectively, which indicates that the spin-coated films are similar regarding electrical conductivity despite a difference in electrode geometry. The *I-V* characteristics from which the thermovoltage was determined were furthermore linear as shown in Fig. C.1 in the supplementary information part C. This indicates that the electrodes are ohmic contacts and the results are therefore not affected by temperature dependent injection. The relatively large error bars shown in Fig. 3d are related to the

noise in the *I-V* characteristics shown in Fig. C.1. To reduce the error, the measured Seebeck coefficient was determined from linear fits of measurements over relatively large voltage intervals of 2 mV.

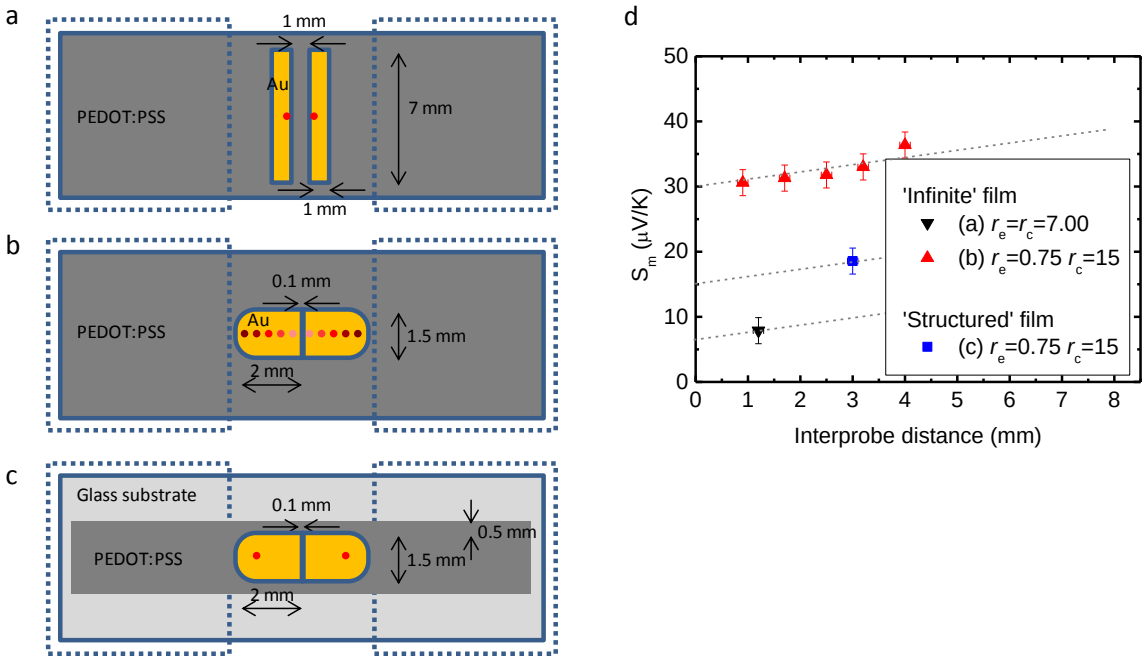

Fig. 3. Schematic representation of (a), (b) unstructured devices with an electrode geometry of (a) r_e = r_c = 7 and (b) r_e = 0.75 and r_c = 15 and a schematic representation of (c) a structured device with an electrode geometry of r_e = 0.75 and r_c = 15. Structuring of PEDOT on the glass substrate is indicated by the different gray tints. The dotted lines indicate the position of the Peltier elements. (d) Experimentally obtained Seebeck coefficient in PEDOT:PSS PH1000 from H.C. Starck for different device geometries as indicated in the legend and shown in (a),(b) and (c). The dashed lines indicate the effect of the Au probes with varying inter-probe distance as indicated by the red dots in (a),(b) and (c). Au contact pads were used.

3.4 Other considerations

In addition to the error in the S_m due to the presence of PEDOT next to the electrodes, also the presence of PEDOT underneath or on top of the metal electrodes results, for the same reasons, in an error in S_m. For the geometry r_c / r_e = L_e / L_c = 24.5, e.g. a device with channel length of 50 µm and electrode length of 1.2 mm, the relative error in S_m was calculated to be 0.18 – 0.40 for PEDOT layer thicknesses of 60 – 180 nm respectively. As the PEDOT under or on top of the electrodes forms an additional, parallel conduction path from electrode to electrode, this relative error may be added to the relative error discussed in Fig. 2.

Also the effect of partial removal of PEDOT *next* to the electrodes was calculated. Referring to Fig. 1, PEDOT was removed starting at a distance 0.4xW_e above and below the electrodes. The relative error in S_m was reduced from ~2 to 0.6 and 0.5 for r_c = 20 and 10, respectively. Experimentally a similar error reduction is observed after partial removal of the PEDOT to ~0.5 mm as shown in Fig. 3c, i.e. equivalent to ~0.33xW_e, above and below the electrodes as shown by the blue square in Fig. 3d.

Next to the overestimation of S_0 by a non-optimal choice in device geometry, also a difference in S_0 between the contact pads and the contact probes can give rise to spurious thermovoltages. Also a

difference in S_0 is possible between, e.g., a thin amorphous film (electrode) and a massive rod (probe) of the same metal. The slope of the orange dashed line in Fig. 3d indicates a difference in S_0 between the ≈ 100 nm Au contact pads and the Au contact probes. The error margins on the data in Fig. 3d preclude making a meaningful estimate for the difference in Seebeck coefficient between probes and pads from the slope of the dashed lines.

Besides the measured Seebeck coefficient also the measured conductivity, σ_m, depends on the shape of the electrodes and the length of the channel. Note that this is the case when σ_m is calculated from the measured current, the applied bias voltage, the channel length and the channel width without taking into account the current outside the channel. The results are shown in Figure 4. The relative error in σ_m compared to the actual conductivity, σ_0, is found to be weakly dependent of the electrode aspect ratio r_e. Square-shaped electrodes (r_e = 1) result in a slightly larger error as opposed to longitudinal electrodes placed parallel of each other (r_e >1). The channel aspect ratio r_c has, however, a stronger influence on the relative error. Placement of the electrodes further apart (i.e. a reduction of r_c) leads to an increase in the relative error. The origin of this is that the conductance of the channel between the electrodes approaches the conductance of pathways outside the channel, which leads to a larger measured conductivity.

The reason why the relative errors in σ_m, Fig. 4, are much smaller than those in S_m, Fig. 2, is quite crucial. In both situations spurious contributions arise from current pathways outside the intended channel, and their relative weight, that is set by the conductance associated with those pathways, is equal in both cases. In the case of Fig. 4 the error is a current that is driven by a constant (applied) voltage over an increasing pathway length. However, in the case of Fig. 2 the driving thermovoltage increases with increasing pathway, c.f. Eq. 1, because of the linear temperature profile.

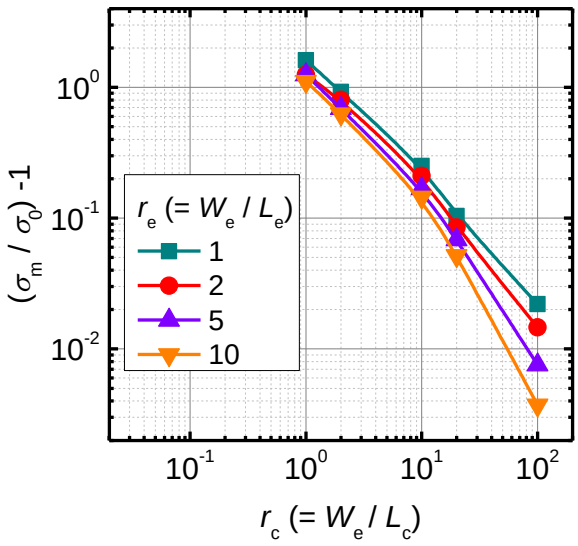

Fig. 4. Relative error in measured conductivity for different channel and electrode aspect ratios.

The results discussed in this paper prove that a detailed specification of the used device geometry is required when reporting the measurement of Seebeck coefficients in films. In for example the references [10, 20, 23-24] no or an unclear description is given of the tested device. It should be noted that the results shown in this paper are also relevant for devices with non-rectangular electrode geometry, such as finite-sized point contacts. For point-like contacts r_e equals 1, which is not optimal regarding the relative error in S_m (see squares in Fig. 2a). To reduce the measurement error (see Fig. 2a) a low value of r_c must be chosen, which is achieved by placing the contacts far away from each other. The cost is, however, a worse signal-to-noise ratio.

4. Conclusions

Overall we have shown that in thin film devices where the active layer is not structured the contact geometry matters a lot to the experimentally obtained Seebeck coefficient, and to a lesser extent to the obtained conductivity. This conclusion is substantiated by numerical and analytical modeling, and experiments. In terms of signal to noise and an accurate determination of the actual Seebeck coefficient, the optimal configuration is a set of parallel, narrow line-shaped electrodes. We found a universal dependence of the relative error on device geometry which allows one to *a posteriori* correct measurement results.

Acknowledgements:

We acknowledge financial support from the Dutch program NanoNextNL.

Supplementary information:

A: Detailed description of the numerical model

To model the thermoelectric transport in PEDOT:PSS a 2D model is used which describes carrier injection and transport based on the Boltzmann transport equation. To model a doped system like PEDOT:PSS, a fixed density of negatively-charged dopants (n_{dopant} = $1 \cdot 10^{25}$ m^{-3}) is added to the semiconductor, compensated by the same density of mobile holes. The model solves the carrier transport equations for electrons, holes, and Poisson's equation by forward integration in time. In this paragraph a detailed description is given on the methods to describe charge transport and carrier injection. Parameters that need to be defined for each calculation are shown in Table A.1.

Table Fel! Ingen text med angivet format i dokumentet.**.1**
Input parameters for the numerical model of a prototypical doped organic semiconductor. Note that the reported relative errors in *S* are independent of the parameters chosen here.

Parameter	Symbol and value
Mobility (electron/hole)	μ_n / μ_p =10^{-7} m^2/Vs
HOMO and LUMO of semiconductor	E_{HOMO} = 5.1 eV; E_{LUMO} = 0 eV
Density of states of semiconductor	N_0 = 0.3 m^{-3}
p-type doping density	n_{dopant} = $1 \cdot 10^{25}$ m^{-3}
Work function of contacts	φ = 5 eV
Relative dielectric constant	ε_r = 3

In the 2D model a rectangular grid is used with grid points at the corners of each cell. The areas of the cells are determined by the widths of the columns and rows which can be specified per row or column. For each cell a material type is specified, either contact or semiconductor. Each cell has its own charge density, exciton density, mobility. Calculations of current, etc. are performed on the grid points. The 4 cells surrounding the grid point are in equilibrium with each other, which is effectuated by area average weighting of these 4 cells. Consequently, a single quasi Fermi level is defined on each grid point.

Carrier transport is described by the Boltzmann transport equation:

$$J_i = -q\mu_i n \nabla \psi_{F,i}, \quad \textbf{(A.1)}$$

where *J* and μ refer to the current density and mobility of the charge carriers; *n* and *p* refer to electron and hole density respectively and as well denote the type of charge carrier when used as subscript. $\psi_{F,i}$ is the quasi Fermi energy for electrons (*i* = *n*) or holes (*i* = *p*), which is given by

$$\psi_{F,n} = \psi_L - \frac{kT}{q} \ln \frac{n}{N_0}, \quad \textbf{(A.2)}$$

$$\psi_{F,p} = \psi_H + \frac{kT}{q} \ln \frac{p}{N_0}, \quad \textbf{(A.3)}$$

where $\psi_L = E_{LUMO} + V$ and $\psi_H = E_{HOMO} + V$, V is the local electrostatic potential, q is the absolute electron charge, k is Boltzmann's constant and T is the local temperature. The continuity equations are

$$\frac{dn}{dt} = \frac{1}{q}\frac{dJ_n}{dx} - R, \quad \textbf{(A.4)}$$

$$\frac{dp}{dt} = -\frac{1}{q}\frac{dJ_p}{dx} - R, \quad \textbf{(A.5)}$$

for electrons and holes, respectively. R is the recombination rate which is described by a Langevin process:[25]

$$R = \frac{q(\mu_n+\mu_p)}{\varepsilon_0\varepsilon_r} pn, \quad \textbf{(A.6)}$$

Carrier injection is described by setting a fixed carrier density at the contacts, n. To describe an ohmic contact for hole injection, n was estimated by assuming thermal activation over a relatively small injection barrier of φ = 0.1 eV: $n = N_0 \exp(-q\varphi/kT)$, where the thermal energy kT was taken at T = 300 K. To determine the electron density at the contacts an electron injection barrier of 5 eV was taken, which effectively switches off electron injection, rendering the device hole-only.

The potential profile throughout the device is calculated from Poisson's equation:

$$\nabla^2 V = -\frac{q}{\varepsilon_0\varepsilon_r}\left(p - n - n_{dopant}\right), \quad \textbf{(A.7)}$$

where ε_0 and ε_r are the dielectric and the relative dielectric constant, respectively.

A simulation is run as follows: No electrons and holes are present in the active layer on initiation except for the holes which compensate the fixed cation density in the modeled semiconductor. At the contacts electrons and holes are present, as prescribed by the boundary conditions. The user-defined bias voltage is applied to one of the contacts and the temperature gradient in the active layer is set as shown in Figure 1. From then on the model calculates the Fermi energy of all the carriers, followed by solving the Boltzmann transport equations. Then electron-hole recombination is accounted for. Consequently the continuity equations are used to calculate the new carrier densities at each gridpoint. A steady-state solution is obtained when the current, which is determined by the sum of current through the contacts, becomes constant.

B: square-counting method

The used, and rather approximate, square-counting method is illustrated in Fig. B1 for electrodes with an aspect ratio r_e = 1 and r_c = 8. Then V_{14} is equal to $16 \cdot V_{23}$. The ratio in conductance can be determined by counting the number of squares in the channel for G_{23} and outside the channel just next to the electrodes for G_{14}. This results, respectively, in 8 squares *parallel* between the electrodes and two times two squares in *series*. This results in $G_{23} = 8\ G_{14}$. Solving Eq. 5 then gives a relative error of 2, consistent with Figure 2b.

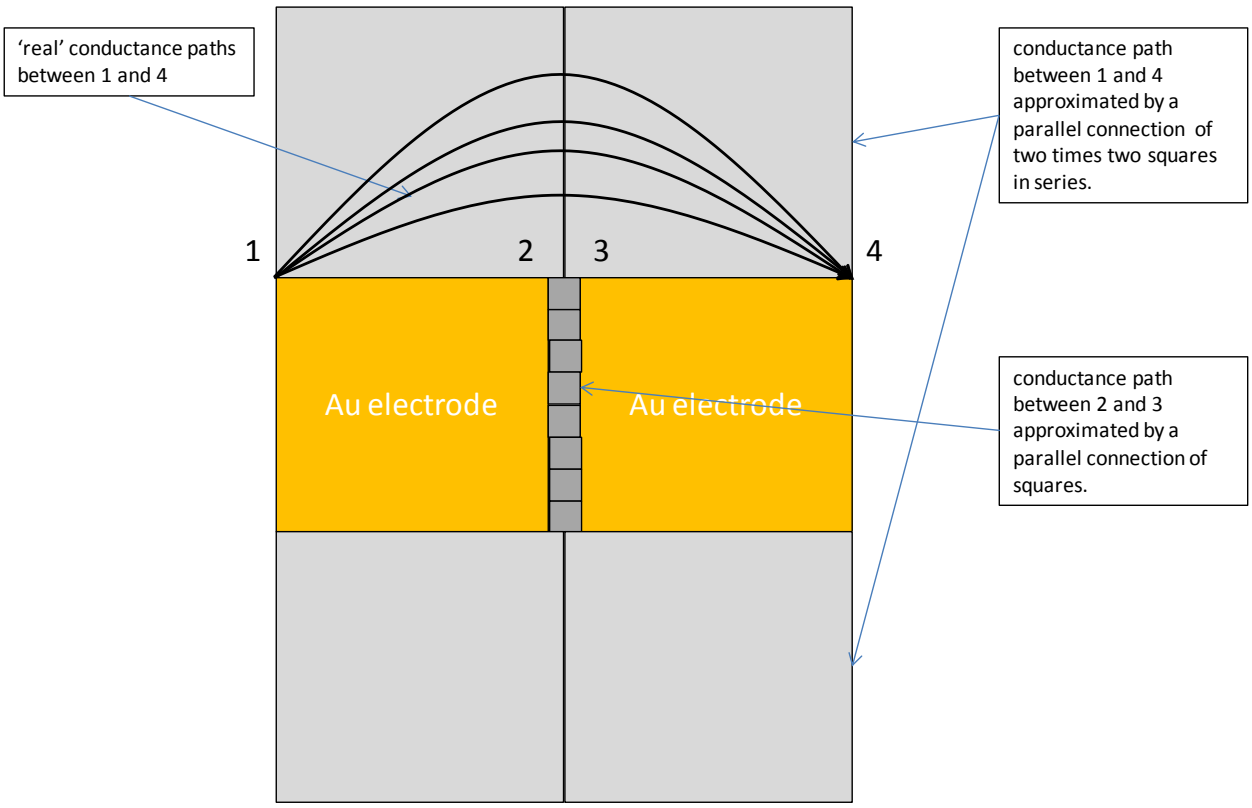

Fig. B1. Schematic of the square-counting method.

C: Typical I-V characteristics for thermovoltage determination

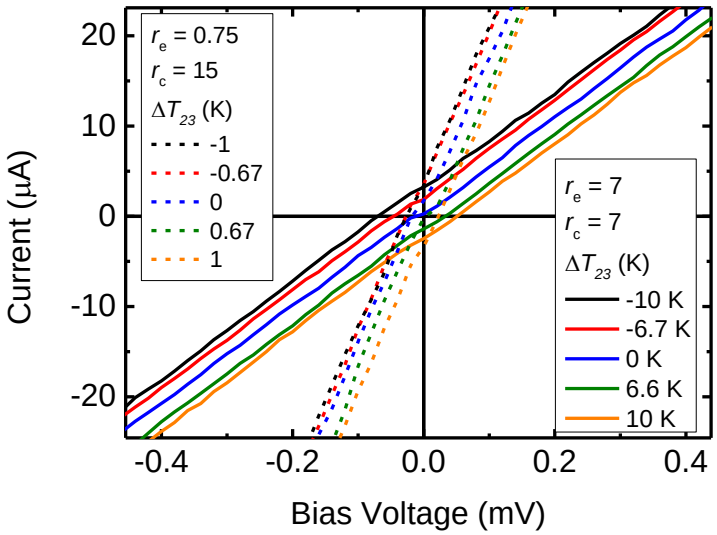

Fig. C1. Typical *I-V* characteristics in PEDOT:PSS (Clevios PH1000) for different electrode geometries as indicated in the legends (see Fig. 3a and b). ΔT_{23} represents the temperature difference across the channel (see Fig. 1).

A distinct, systematic offset of the *I-V* curves along the voltage axis (around a bias of 0 mV) is present with a to us unknown origin. The offset is systematic in position and range (~50 µV) and the *I-V* curves are measured over a large voltage region (2000 µV). Linear fits from these curves were used to determine the temperature dependent thermovoltage, which cancels out the effect of the systematic offset. Consequently, the offset has no significant effect on the determined Seebeck coefficient. The latter was confirmed by evaluating the Seebeck coefficient from the parts of the I-V curves at positive or negative bias.

References:

1 N. Dubey and M. Leclerc, J Polym Sci Pol Phys **49**, 467 (2011).
2 O. Bubnova, Z. U. Khan, A. Malti, S. Braun, M. Fahlman, M. Berggren, and X. Crispin, Nat. Mater. **10**, 429 (2011).
3 G. H. Kim, L. Shao, K. Zhang, and K. P. Pipe, Nat. Mater. **12**, 719 (2013).
4 W. C. Germs, K. Guo, R. A. J. Janssen, and M. Kemerink, Phys. Rev. Lett. **109**, 016601 (2012).
5 O. Bubnova, M. Berggren, and X. Crispin, J. Am. Chem. Soc. **134**, 16456 (2012).
6 O. Bubnova and X. Crispin, Energ Environ Sci **5**, 9345 (2012).
7 O. Bubnova, et al., Nat. Mater. **13**, 190 (2014).
8 K. P. Pernstich, B. Rossner, and B. Batlogg, Nat. Mater. **7**, 321 (2008).
9 S. K. Yee, N. E. Coates, A. Majumdar, J. J. Urban, and R. A. Segalman, PCCP **15**, 4024 (2013).
10 T.-C. Tsai, H.-C. Chang, C.-H. Chen, Y.-C. Huang, and W.-T. Whang, Org. Electron. **15**, 641 (2014).
11 J. Wusten and K. Potje-Kamloth, J Phys D Appl Phys **41**, 135113 (2008).
12 B. Zhang, J. Sun, H. E. Katz, F. Fang, and R. L. Opila, Acs Appl Mater Inter **2**, 3170 (2010).
13 N. Toshima and N. Jiravanichanun, J. Electron. Mater. **42**, 1882 (2013).
14 Y. Hiroshige, M. Ookawa, and N. Toshima, Synth. Met. **157**, 467 (2007).
15 R. R. Yue and J. K. Xu, Synth. Met. **162**, 912 (2012).
16 J. Y. Kim, J. H. Jung, D. E. Lee, and J. Joo, Synth. Met. **126**, 311 (2002).
17 D. Djurek, D. Jerome, and K. Bechgaard, J Phys C Solid State **17**, 4179 (1984).
18 D. Nemir and J. Beck, J. Electron. Mater. **39**, 1897 (2010).
19 T. Park, C. Park, B. Kim, H. Shin, and E. Kim, Energ Environ Sci **6**, 788 (2013).
20 D. Kim, Y. Kim, K. Choi, J. C. Grunlan, and C. H. Yu, Acs Nano **4**, 513 (2010).
21 K. C. See, J. P. Feser, C. E. Chen, A. Majumdar, J. J. Urban, and R. A. Segalman, Nano Lett. **10**, 4664 (2010).
22 G. D. Mahan and J. O. Sofo, Proceedings of the National Academy of Sciences of the United States of America **93**, 7436 (1996).
23 F. X. Jiang, J. K. Xu, B. Y. Lu, Y. Xie, R. J. Huang, and L. F. Li, Chinese Phys Lett **25**, 2202 (2008).
24 F. F. Kong, C. C. Liu, J. K. Xu, Y. Huang, J. M. Wang, and Z. Sun, J. Electron. Mater. **41**, 2431 (2012).
25 M. P. Langevin, Ann. Chim. Phys. **28**, 433 (1903).